



Clarifying the critical roles of iron in boosting oxygen reduction: Single Fe atoms anchored on carbon vacancies as efficient active sites

Feng Tan ^{a,b}, Wei Li ^{a,b}, Jingsong Wang ^a, Chungang Min ^b, Zhanping Li ^c, Bingsen Zhang ^d,
Xusheng Zheng ^e, Lina Li ^f, Longzhou Zhang ^g, Liexing Zhou ^b, Qingnan Shi ^a, Xikun Yang ^{a,b,*}

^a Faculty of Materials Science and Engineering, Kunming University of Science and Technology, Kunming 650093, China

^b Research Center for Analysis and Measurement, Kunming University of Science and Technology, Kunming 650093, China

^c Analysis Center Tsinghua University, Tsinghua University, Beijing 100080, China

^d Shenyang National Laboratory for Materials Science, Institute of Metal Research Chinese Academy of Sciences, Shenyang 110016, China

^e National Synchrotron Radiation Laboratory (NSRL), University of Science and Technology of China, Hefei 230029, China

^f Shanghai Synchrotron Radiation Facility, Shanghai Institute of Applied Physics, Chinese Academy of Sciences, Shanghai 201204, China

^g Faculty of Materials Science and Engineering, Yunnan University, Kunming 650091, China



ARTICLE INFO

Keywords:

Structurally-defined precursor
Single iron atom
Carbon vacancy
Catalytic active site
Oxygen reduction reaction

ABSTRACT

Due to highly heterogeneity of pyrolyzed transition metal-nitrogen-carbon (M-N-C) catalyst, elucidating mechanisms of roles of metal in enhancing oxygen reduction reaction (ORR) is challenging. Here, we design a surface structurally-defined precursor with Fe-N coordination to atomically disperse iron (Fe) on N-doped carbon hollow microspheres surface (NHMs@Fe) by pyrolysis of the precursor. The obtained NHMs@Fe catalyst exhibits a high ORR activity comparable to commercial Pt/C catalyst. The detailed analyses confirmed that (i) Fe atoms are uniformly distributed on N-poor carbon surface, and (ii) the designed Fe-N_x coordination are destroyed and don't convert into Fe-N_x active sites after thermal activation. We find that single Fe atoms produced by carbothermal reduction are directly trapped into adjacent carbon vacancies generated by the removal of N to create active sites for ORR. This work not only reveals the origin of activity of Fe-N-C catalyst but also opens an avenue for preparation of high-performance M-N-C catalysts.

1. Introduction

Carbon-based non-noble metal ORR catalysts, represented by the M-N-C catalysts (M=Fe, Co and Cu etc.), have been developed as the most promising candidates to replace Pt-based catalysts in important applications such as fuel cells and metal-air batteries [1–12]. The M-N-C catalysts are mainly derived from the pyrolysis of precursors containing carbon, nitrogen and transition salts [1–7,10–20]. During the pyrolysis process, the precursors are first decomposed at high temperatures and then graphene-like graphitic layers and various metal species, including metal oxide [14,20], metal carbide [7,13,16] and the proposed M-N_x active sites [10–20], are formed. Meanwhile, active N species, such as pyridinic-N and graphitic-N, are generated due to the incorporation of N into the carbon ring [4,17–19]. In addition, various porous carbon [1,4, 13,19] and carbon defects [21–24] are also produced. Thus, pyrolyzed M-N-C catalysts are inherently structurally and compositionally heterogeneous carbon materials, and the roles of metal in the catalysts

synthesis involve the active site formation, N-doped, and associated carbon structure and defect.

Among various M-N-C catalysts, the pyrolyzed Fe-N-C catalyst performs best [2,5–7,15]. The high ORR activity of this catalyst is believed to come from the formation of Fe-N_x or porphyrin-like Fe-N₄ active sites in the pyrolysis [12–20]. However, the structure of active sites for the Fe-N-C catalyst remains elusive. For example, in the absence of Fe-N_x coordinated active sites, the pyrolyzed Fe-based catalysts prepared by using Fe-doped zeolitic imidazolate framework (ZIF)-8 precursors still show high ORR activity comparable with Pt/C catalyst [25]. Furthermore, trace metal in the N-doped carbon, possibly present in the form of a single atom, have been considered to have a profound effect on catalytic activity, which leads to the fact that the roles of metal in dramatically increasing the ORR activity is still a controversial issue [26–28]. The debate focuses on whether the iron ions are involved in the active sites [12–20] or merely promote the formation of active sites [4,29,30]. These controversial results make us realize that understanding of Fe's

* Corresponding author at: Faculty of Materials Science and Engineering, Kunming University of Science and Technology, Kunming 650093, China.
E-mail address: yxk630@hotmail.com (X. Yang).

role in improving oxygen reduction requires a detailed study of Fe's influence on key factors such as active site formation, N doping, and associated carbon structure and defects. Unfortunately, the complex structural recombination of Fe-N-C catalysts in the high temperature pyrolysis process leads to the inhomogeneity of catalyst particles inside and outside, making it very difficult to thoroughly uncover the mechanisms of the roles of Fe in enhancing ORR activity even with advanced characterization techniques, which is the exact bottleneck that hinders the further development of Fe-N-C catalysts.

In order to solve these problems, a surface science approach can be used as a reference to construct a structure-activity relationship for the carbon-based catalysts [31]. Traditional methods for investigating the composition and structure of catalysts (such as the atomic steps, ledges, kinks, and atomic structure of the active site) have been employed for well-defined surfaces such as metallic single crystals [32,33] and layered materials [34]. The structure-activity relationship and catalytic mechanism of these materials are demonstrated in depth by using surface-sensitive characterization methods. Similar approaches are also suitable for carbon-based catalysts without metal species. For example, the active sites of N-doped carbon catalysts have been characterized with model catalysts, which are obtained from controllable doping of N species on the surface of highly oriented pyrolytic graphite (HOPG) with N^+ ion beam etching [35]. However, such a physical approach is unavailable for applying Fe^{+} -ion beams to building active sites related to Fe-N species on HOPG as model catalysts. Hence, the Fe-N-C catalysts should be engineered to contain a high density of active Fe atoms on the surface, which is conducive to the study of structure-activity relationship by using surface-sensitive techniques, and further reveal the key role of Fe in improving oxygen reduction.

Here, we first synthesized polyphenylenediamine hollow microspheres (PHMs) with well-defined $Fe-N_x$ content on their surface as a surface structurally-defined precursor. Then, highly efficient single Fe atoms were uniformly distributed on the surface of the N-doped carbon hollow microspheres (NHMs) after the carbonization of the precursor. The optimized NHMs@Fe catalyst (carbonization at 900 °C) shows high catalytic activity for ORR with a half-wave potential ($E_{1/2}$) of 0.912 V in a 0.1 M KOH solution, 61 mV higher than that of Pt/C (0.851 V). Based on analytical results from surface-sensitive techniques, electrochemical methods and theoretical calculations, our studies show that (i) a high performance surface structure for ORR is built by the implantation and migration of Fe atoms on N-doped carbon, (ii) the $Fe-N_x$ complex does not convert into the proposed $Fe-N_4$ site during thermal activation, but instead generates Fe atom through carbothermal reduction, and the Fe atom is trapped in N-removed carbon vacancy to form stable single Fe atom, and (iii) single Fe atoms distributed on a N-poor carbon surface are the most effective catalytic sites.

2. Experimental section

2.1. Reagents and chemicals

The m-phenylenediamine (99.5%), iron chloride hexahydrate ($FeCl_3 \cdot 6H_2O$, 99%) and ammonium persulfate ($(NH_4)_2S_2O_8$, 99.99% metals basis) were obtained from Aladdin Reagent (Shanghai, China). Commercial Pt/C catalyst (20 wt%) was bought from Johnson Matthey. All aqueous solutions were prepared with deionized (DI) water (~18 $M\Omega \cdot cm$) from HITECH laboratory water purification system. Unless otherwise stated, all the reagents were of analytical grade and were used as received without further purification.

2.2. Preparation of NHMs and NHMs@Fe catalysts

In a typical procedure, the poly (phenylenediamine) hollow microspheres (PHMs) were synthesized by a modified oxidative polymerization of m-phenylenediamine monomer route. In a typical experimental procedure, 1.5 g of m-phenylenediamine monomer was dissolved in 10

mL of deionized water and the mixed solution was dispersed with ultrasound at 0–5 °C for 30 min. Then, 6 mL of 1.67 M $(NH_4)_2S_2O_8$ aqueous solution was added into the above mixed solution with constant stirring for 1 min. The suspension was kept at 10 °C for 24 h. The precipitate was filtered and washed with deionized water for three times, then dried at 60 °C for 24 h under vacuum to produce the PHMs. To prepare the NHMs@Fe, 0.2 g of PHMs was added into the 10 mL of 0.06 g mL^{-1} $FeCl_3 \cdot 6H_2O$ aqueous solution and then the mixed solution was dispersed for 30 min with ultrasonic. The suspension was stirred for 72 h at 30 °C. The precipitate was filtered and washed with deionized water for three times, then dried at 60 °C for 24 h under vacuum to obtain PHMs@Fe-N. Finally, the NHMs@Fe catalyst with trace iron (0.21 wt% Fe) was fabricated by carbonization of the PHMs@Fe-N at 900 °C under nitrogen gas for 2 h. For comparison, the NHMs catalyst consisted of N-doped carbon hollow microspheres was prepared by carbonization of PHMs at 900 °C. In addition, the NHMs@Fe-N were heat-treated at the desired temperatures (700 °C, 800 °C, 900 °C and 950 °C) under nitrogen gas for 2 h and corresponding catalysts were denoted as NHMs@Fe-700, NHMs@Fe-800, NHMs@Fe-900 and NHMs@Fe-950 respectively.

2.3. Characterization

SEM images and SEM images under back-scattering electron detector mode were obtained from a Nova Nano 450. TEM images were obtained from a Tecnai G² TF30 S-Twin with an acceleration voltage of 100 kV. Bright-field and HAADF images were collected from a aberration-corrected JEOL ARM200F with a guaranteed resolution of 0.08 nm. Raman spectra were recorded on a RENISHAW in Via instrument with an Ar laser source of 488 nm in a macroscopic configuration. XPS measurements were performed on a PHI-5000 VersaProbe II, all binding energies of core level spectra were corrected to the C 1s peak at 284.8 eV. XAFS spectra at the Fe K edge ($E_0 = 7112$ eV) was conducted at the BL11B beamline of Shanghai Synchrotron Radiation Facility (SSRF). The energy was corrected on the basis of the absorption edge of pure Fe foil. Fe K-edge extended x-ray absorption fine structure (EXAFS) data were analyzed using standard procedures with the program IFEFFIT. ToF-SIMS measurement was performed on the ToF.SIMS 5 (ION-TOF) with a reflectron type ToF analyzer. SRPES experiments were performed at the photoemission end-station at beamline BL10B in the National Synchrotron Radiation Laboratory (NSRL) in Hefei, China.

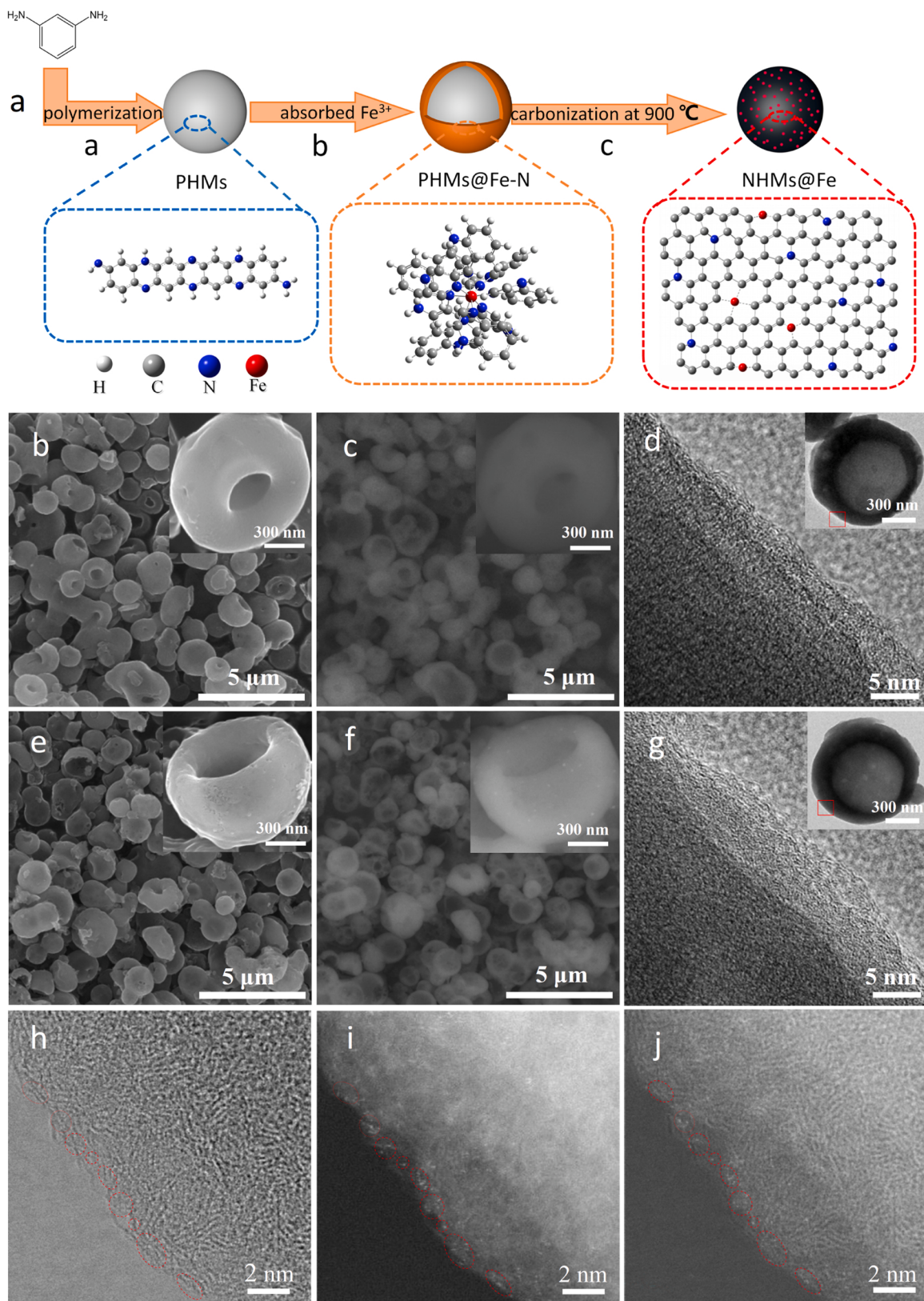
2.4. Electrochemical measurements

All the electrochemical tests were performed in a conventional three-electrode system on an electrochemical workstation (CHI 760E), using a platinum plate as the counter electrode, a Ag/AgCl as the reference electrode, and a glassy carbon electrode coated with the as-prepared catalysts' ink was used as the working electrode. All the potentials measured with an Ag/AgCl electrode was converted to potential versus RHE according to $E(RHE) = E(Ag/AgCl) + 0.0592 \times pH + 0.2046V$. To prepare the working electrode, 6 mg of a catalyst was added into a solution containing 950 μL isopropanol, and 50 μL Nafion (5%). The solution was ultrasonicated for 30 min to obtain a homogeneous suspension ink at the catalyst concentration of about 6 $mg mL^{-1}$. 20 μL ink of the suspension was loaded on polished glassy carbon electrode to get the catalyst loading of 0.611 $mg cm^{-2}$.

3. Results and discussion

3.1. Structural analysis of the precursor

A surface coordination chemistry approach was proposed to synthesize surface structurally-defined precursor with Fe-N coordination, as shown in Fig. 1a. First, the PHMs were synthesized by an oxidative polymerization of m-phenylenediamine monomer, and then the



(caption on next page)

resultant PHMs were dipped in a solution of ferric chloride so that Fe³⁺ ions in the solution were absorbed on the PHM surface (Supporting 1). In order to confirm the formation of Fe-N coordination on the PHM, the

chemical adsorption of Fe³⁺ ions on nitrogen-containing groups of PHMs surface was confirmed by X-ray photoelectron spectroscopy (XPS, see Fig. S3), and the bond distance of Fe-N and coordination number around

Fig. 1. Synthesis of NHMs@Fe via carbonization of structurally-defined precursor with Fe-N coordination and characterization of morphology and structure for NHMs and NHMs@Fe. (a) Schematic diagram of the synthetic process for NHMs@Fe catalyst. Firstly, PHMs were synthesized by the oxidative polymerization of m-phenylenediamine monomer, and then Fe^{3+} ions are absorbed on the PHM surface to form Fe-N chelate complexes by coordination between Fe and N. Finally, NHMs@Fe catalyst was fabricated by carbonization of the PHMs@Fe-N. (b) SEM images of NHMs (inset: HRSEM image of a typical microsphere in the NHMs), and (c) corresponding SEM images of NHMs under back-scattering electron detector (inset: corresponding HRSEM image of the microsphere under back-scattering electron detector). (d) HRTEM image of individual microsphere in the NHMs (inset: TEM image of the microsphere). (e) SEM images of NHMs@Fe (inset: HRSEM image of a typical microsphere in the NHMs@Fe), and (f) corresponding SEM images of NHMs@Fe under back-scattering electron detector (inset: corresponding HRSEM image of the microsphere under back-scattering electron detector). (g) HRTEM image of individual microsphere in the NHMs@Fe (inset: TEM image of the microsphere). (h) High-resolution BF-STEM image showing partially graphitized carbon fringes and defects on the edges of a typical microsphere in the NHMs@Fe. (i) corresponding HAADF-STEM image exhibiting dispersion of single Fe atoms in the subnanometer region at the edge of the microsphere (sizes of the bright spots are $\sim 0.2 \text{ nm}$). (j) BF+HAADF overlapping image depicting occupation of defective sites by single Fe atoms.

Fe atoms were determined by X-ray absorption spectroscopy (XAS, see Table S2). Furthermore, 11 fragment ions related with the Fe-N were identified by time-of-flight secondary ion mass spectrometry (ToF-SIMS, see Fig. S7). Based on the results of XPS, XAS and ToF-SIMS and theoretical computations, Fe^{3+} ions are only coordinated with imine N of poly (phenylenediamine) chains to form stable Fe-N_8 chelate structure (Fig. S11). Therefore, the PHMs covered by the Fe-N chelate complexes could serve as a surface structurally-defined precursor, denoted as PHMs@Fe-N.

3.2. Atomic dispersion of Fe on N-doped carbon surface

Scanning electron microscopy (SEM) images show that both PHMs and PHMs@Fe-N have a hollow microsphere shape, and some of them present a small open hole in the center of the sphere (Fig. S12). After PHMs and PHMs@Fe-N are carbonized at 900°C , the obtained NHMs and NHMs@Fe still retain the shape of a hollow microsphere (Figs. 1b, e and S13). It is clearly observed with high-resolution SEM (HRSEM) that the surface of NHMs is even smoother than that of NHMs@Fe (see inset in Fig. 1b, e). In particular, a few bright spots are observed (see inset in Fig. 1f) in the corresponding HRSEM images of NHMs@Fe in a back-scattering electron detector mode, while similar bright spots were not observed in the HRSEM images corresponding to NHMs (see inset in Fig. 1c). These bright spots are metallic iron nanoparticles according to the principle of element contrast.

Transmission electron microscopy (TEM) was employed to investigate the microstructure of NHMs and NHMs@Fe, the TEM images also exhibit the structure of a hollow microsphere (see inset in Fig. 1d, g). Furthermore, the edges of individual microspheres in both NHMs and NHMs@Fe are observed with high-resolution transmission electron microscopy (HRTEM), the HRTEM images show that there is an obvious carbon layer at these edges (Fig. 1d, g), and this carbon layer is mainly composed of flake-like graphite and highly defective layered graphitic material. However, microstructural differences in the carbon layers of NHMs and NHMs@Fe cannot be distinguished through lattice fringes.

To further reveal the atomic-scale microstructure of the carbon layers, we used aberration-corrected scanning transmission electron microscopy (AC-STEM) to inspect the edge of a typical microsphere in NHMs@Fe. A high resolution bright-field (BF)-STEM image (Figs. 1h and S15b) shows partially graphitized carbon fringes and many defects on the edges of the microsphere (as indicated by red dotted circles). Unexpectedly, when the same region is observed with a high-angle annular dark field (HAADF)-STEM, many single Fe atoms (marked by red circles) can be clearly observed in the subnanometer region at the edge of the microsphere (Figs. 1i and S15a). The homogeneous distribution of single Fe atoms on the surface of NHMs@Fe is ascribed to the fact that an iron ion in the PHMs@Fe-N precursor is coordinated with eight nitrogen atoms to form a stable Fe-N_8 structure, which helps to prevent Fe atoms from aggregating during carbonization of the precursor.

More importantly, the overlapping high-magnification image (BF+HAADF, Fig. 1j) shows that the single Fe atoms only occupy defective sites, as witnessed in the BF image (Fig. 1h), rather than intercalation sites between the graphene sheets. The above suggests that

single Fe atoms are trapped in the graphitic defects to form stable single Fe atoms. Furthermore, the existence of these defects is also supported by the high I_D/I_G intensity ratio (1.85) of NHMs@Fe, as shown in the Raman spectrum (Fig. S17).

3.3. Effect of Fe on composition and structure of N-doped carbon surface

To understand the effect of atomically dispersed Fe on the N-doped carbon surface, the distribution of N from the near surface to the surface on the NHMs and NHMs@Fe was investigated by synchrotron radiation photoemission spectroscopy (SRPES) (Fig. 2a–d and Supporting 15). SRPES data obtained with photon energies of 1253.6 eV (analysis depth $\sim 37 \text{ \AA}$) show that the N content of NHMs (3.3 at%) is slightly higher than that of NHMs@Fe (1.8 at%) within the near-surface regions. However, SRPES data obtained with photon energies of 500 eV (analysis depth $\sim 11 \text{ \AA}$) show that the N content of NHMs (14.3 at%) is much higher than that of NHMs@Fe (4.7 at%) within the surface regions. A large enhancement of the N concentration on the NHMs surface is caused by the segregation of N atoms to the surface at high temperatures, which is a common physical phenomenon in alloys or materials containing impurities [34,36–38]. These results indicate that the atomically dispersed Fe significantly promotes the N loss on the N-doped carbon surface.

The pore size distribution and specific surface area of the NHMs and NHMs@Fe were determined by the Brunauer-Emmett-Teller (BET), as shown in Fig. 2e–f. It can be seen that the specific surface area of NHMs and NHMs@Fe is $\sim 1576 \text{ m}^2 \text{ g}^{-1}$ and $\sim 1837 \text{ m}^2 \text{ g}^{-1}$ respectively, indicating that the NHMs and NHMs@Fe had very high specific surface area. Furthermore, the type I isotherms of NHMs and NHMs@Fe confirm that the porosity is made up of micropores exclusively. The micropores in NHMs and NHMs@Fe are generated by the removal of N at high temperatures, which is mainly due to the conversion of low specific surface area nitrogenous precursors (see Fig. S12e–f) into high specific surface area carbon materials after carbonization. In addition, the specific surface area for NHMs@Fe ($\sim 1837 \text{ m}^2 \text{ g}^{-1}$) is slightly greater than that of the NHMs ($\sim 1576 \text{ m}^2 \text{ g}^{-1}$) due to N loss caused by atomic Fe. Thus, atomically dispersed Fe increases the specific surface area of NHMs@Fe but has no effect on its pore structure.

3.4. Electrocatalytic performance for ORR

In order to determine the contribution of atomic Fe on the N-doped carbon surface to ORR, the ORR activities of the NHMs and NHMs@Fe catalysts were first evaluated using a rotating ring-disk electrode (RRDE) measurement in 0.1 M KOH and 0.5 M H_2SO_4 solution saturated with O_2 , and compared with a commercial Johnson Matthey Pt/C catalyst (20 wt% Pt), as shown in Fig. 3a and b. The linear sweep voltammetry (LSV) results indicated that the NHMs catalyst showed a half-wave potential ($E_{1/2}$) of 0.755 V in 0.1 M KOH (Fig. 3a) and 0.342 V in 0.5 M H_2SO_4 (Fig. 3b). However, in an alkaline medium, the NHMs@Fe catalyst exhibited an $E_{1/2}$ of 0.912 V, 157 mV higher than the NHMs catalyst, and 61 mV higher than Pt/C (Fig. 3a), the most positive among the current state-of-the-art Fe-N-C catalysts in alkaline medium (Table S9). In particular, its mass activity ($4.2 \text{ A mg}^{-1}\text{Fe}$ at 0.90 V vs

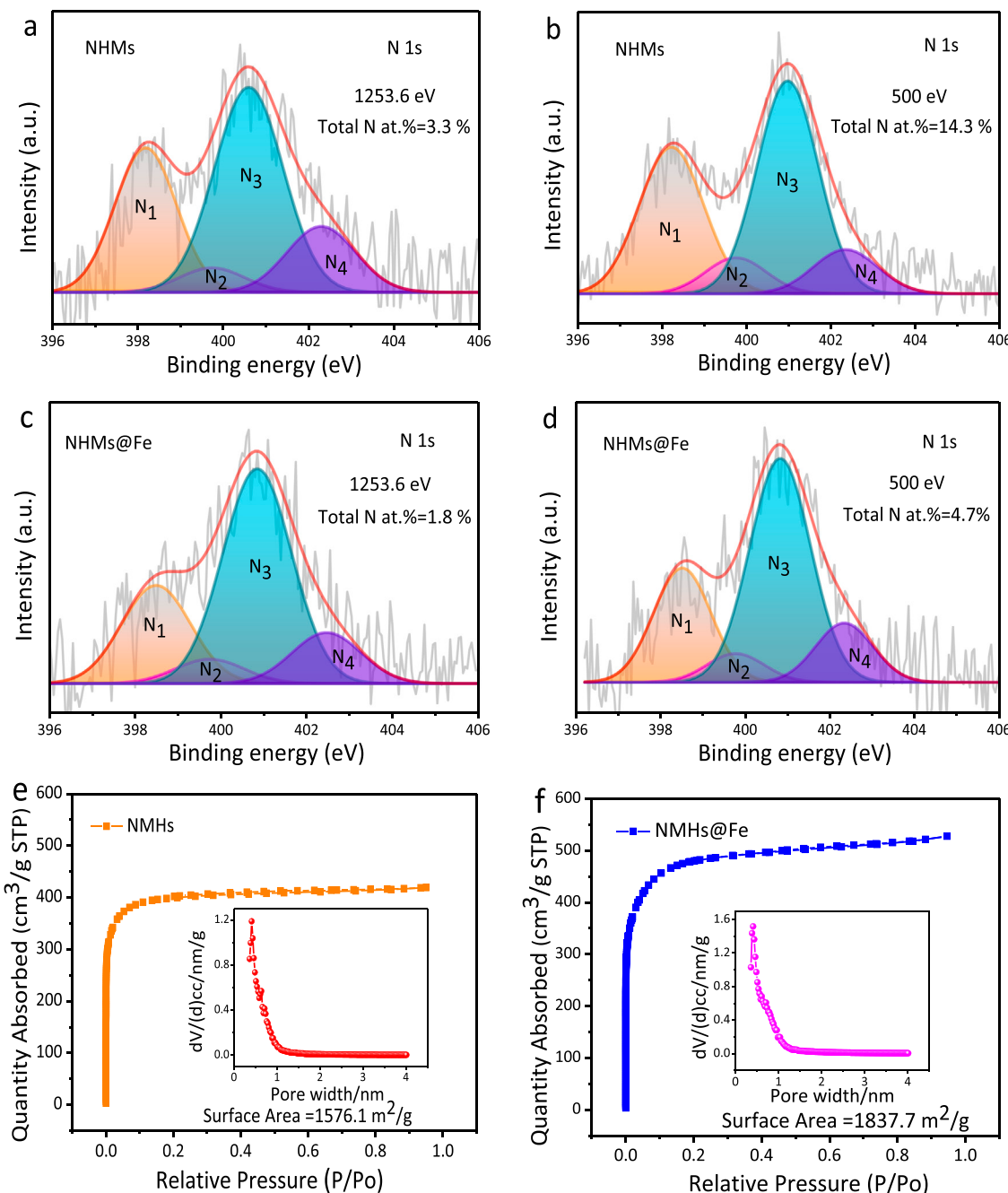


Fig. 2. Composition depth profiles and pore structure. (a, b) SRPES N1s spectra of NHMs measured with photon energies of 1253.6 eV (a) and 500 eV (b). (c, d) SRPES N1s spectra of NHMs@Fe measured with photon energies of 1253.6 eV (c) and 500 eV (d). (e) N₂ adsorption/desorption isotherm of NHMs (inset: pore size distribution of NHMs); (f) N₂ adsorption/desorption isotherm of NHMs@Fe (inset: pore size distribution of NHMs@Fe). (N₁, N₂, N₃ and N₄ are corresponding to pyridine N, pyrrole N, graphite N and oxidized N, respectively).

RHE) is enhanced 84-fold compared with that of the commercial Pt/C catalyst ($0.05 \text{ A mg}^{-1} \text{ Pt}$). In an acidic medium, the NHMs@Fe catalyst exhibited an $E_{1/2}$ of 0.750 V, 408 mV higher than the NHMs catalyst, and only 15 mV lower than the Pt/C (Fig. 3b). Furthermore, to reveal the role of Fe during the ORR process, the ORR kinetics for the NHMs and NHMs@Fe catalysts were also evaluated by using the Koutecky-Levich equation. The results indicate that the ORR process for the NHMs catalyst is dominated by a two-electron reduction pathway (Fig. S18e, f), whereas the NHMs@Fe catalyst exhibits a direct four-electron reduction pathway in both alkaline and acid media (Fig. 3c, d). This indicates that the stable presence of a large number of single Fe atoms on the N-doped carbon converts the N-doped carbon from a two-electron reduction

pathway to a four-electron reduction pathway. Moreover, the results of an accelerated durability test indicate that after 10,000 cycles, the $E_{1/2}$ of the NHMs@Fe catalyst has negative potential shifts of ~ 25 mV in alkaline medium (Fig. 3e) and negative potential shifts of ~ 43 mV in acidic medium (Fig. 3f), indicating that the NHMs@Fe catalyst has a superior long-term stability.

The NHMs catalyst shows an apparently high ORR activity, which is mainly due to abundant pyridinic-N [35,44] and graphitic-N [28,43] in the NHMs as active sites (Table S4). In particular, the N content on the surface of the NHMs (14.3 at%) is much higher than that of NHMs@Fe (4.7 at%) due to surface segregation of N atoms, resulting in a higher ratio of pyridine-N and graphite-N of NHMs than that of NHMs@Fe

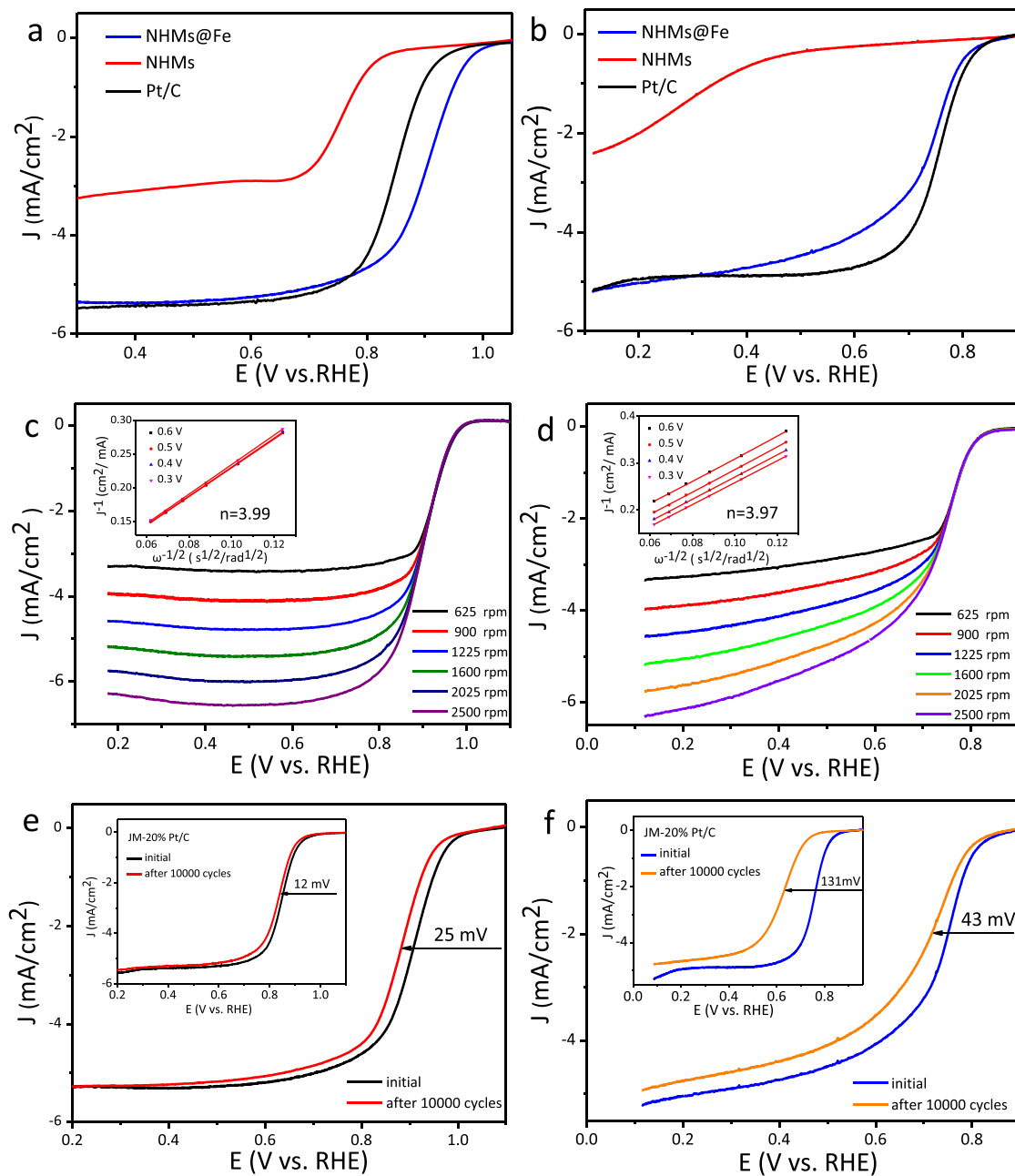


Fig. 3. ORR performance of the NHMs, NHMs@Fe and Pt/C catalysts. (a, b) LSV curves of the NHMs, NHMs@Fe and Pt/C catalysts in O₂-saturated (a) 0.1 M KOH and (b) 0.5 M H₂SO₄ (rotation rate 1600 rpm, scan rate 10 mV s⁻¹). (c, d) LSV curves of ORR of NHMs@Fe catalyst obtained at different rotating rates in (c) 0.1 M KOH and (d) 0.5 M H₂SO₄ (The insert is K-L plots of current density reciprocal (j^{-1}) versus $\omega^{-1/2}$ at different potentials on NHMs@Fe electrode). (e, f) Steady-state ORR polarization curves of NHMs@Fe before and after 10,000 potential cycles in O₂-saturated (e) 0.1 MKOH and (f) 0.5 M H₂SO₄ (insert: steady-state ORR polarization curves of Pt/C).

(Table S4). Moreover, although optimizing the pore size and distribution of catalyst can promote the mass transport for ORR [1,4,12], the porosity of both NHMs and NHMs@Fe are composed of micropores exclusively. Therefore, the NHMs@Fe catalyst shows significantly higher ORR activity than the NHMs catalyst, which obviously cannot be completely attributed to the contribution of total N content and pore structure for ORR. Based on these results, we can infer that the atomically dispersed Fe on the N-poor surface play a key role in promoting electrocatalytic performance.

3.5. Identification of active sites for ORR

To reveal the origin of high activity for the NHMs@Fe catalyst, it is

very important to determine the structure of active center associated with Fe. Currently, the identification of active sites for ORR in the pyrolyzed M-N-C catalysts can be obtained not only by curve fitting of XAS data [5,13,14,19,20], but also by direct measurement of ToF-SIMS [39, 40]. Previously, our group employed the XAS technique, especially in combination with direct ToF-SIMS analytical technique, to successfully identify the Cu-N₄ coordination structure in a Cu-N₄-C catalyst synthesized by a hydrothermal method [41]. Here, we first used the XAS technique to determine the chemical state and coordination environment of the center Fe atoms in NHMs@Fe, and have selected Fe foil, iron phthalocyanine (FePc) and Fe₂O₃ as references, as shown in Fig. S23a and b. Fig. S23a shows Fe K-edge X-ray absorption near the edge structure (XANES) spectra of NHMs@Fe, Fe foil, FePc and Fe₂O₃. It can

be seen that the absorption edge of NHMs@Fe has a clear shift towards the higher energy region in comparison to Fe foil and FePc, closer to that of Fe_2O_3 . In addition, the appearance of the pre-edge feature at ~ 7113 eV indicates that the Fe center in the NHMs@Fe has a non-square planar configurations through an axial ligation due to the presence of axial ligand(s) (commonly bridging O and/or hydroxyl) [42]. Fitting of the EXAFS spectrum for FePc gives a Fe-N bond distance of 1.91 ± 0.02 Å and coordination number of 4.2 ± 0.5 (Fig. S4c and

Table S2), corresponding exactly to a plane-symmetric $\text{Fe}-\text{N}_4$ coordination structure. However, the peak for NHMs@Fe can be only fit well with an Fe-O path with the low-coordinated Fe-O species (bond distance of 1.85 ± 0.05 Å and coordination number of 2.3 ± 0.8) and the tetrahedral Fe-O species [20] (bond distance of 2.00 ± 0.02 Å and coordination number of 4.2 ± 1.1) (Fig. S23c and Table S6), suggesting that the Fe environment in NHMs@Fe is confirmed to be Fe-O rather than Fe-N_x, similar to previous results reported by Mukerjee et al. that no Fe-N

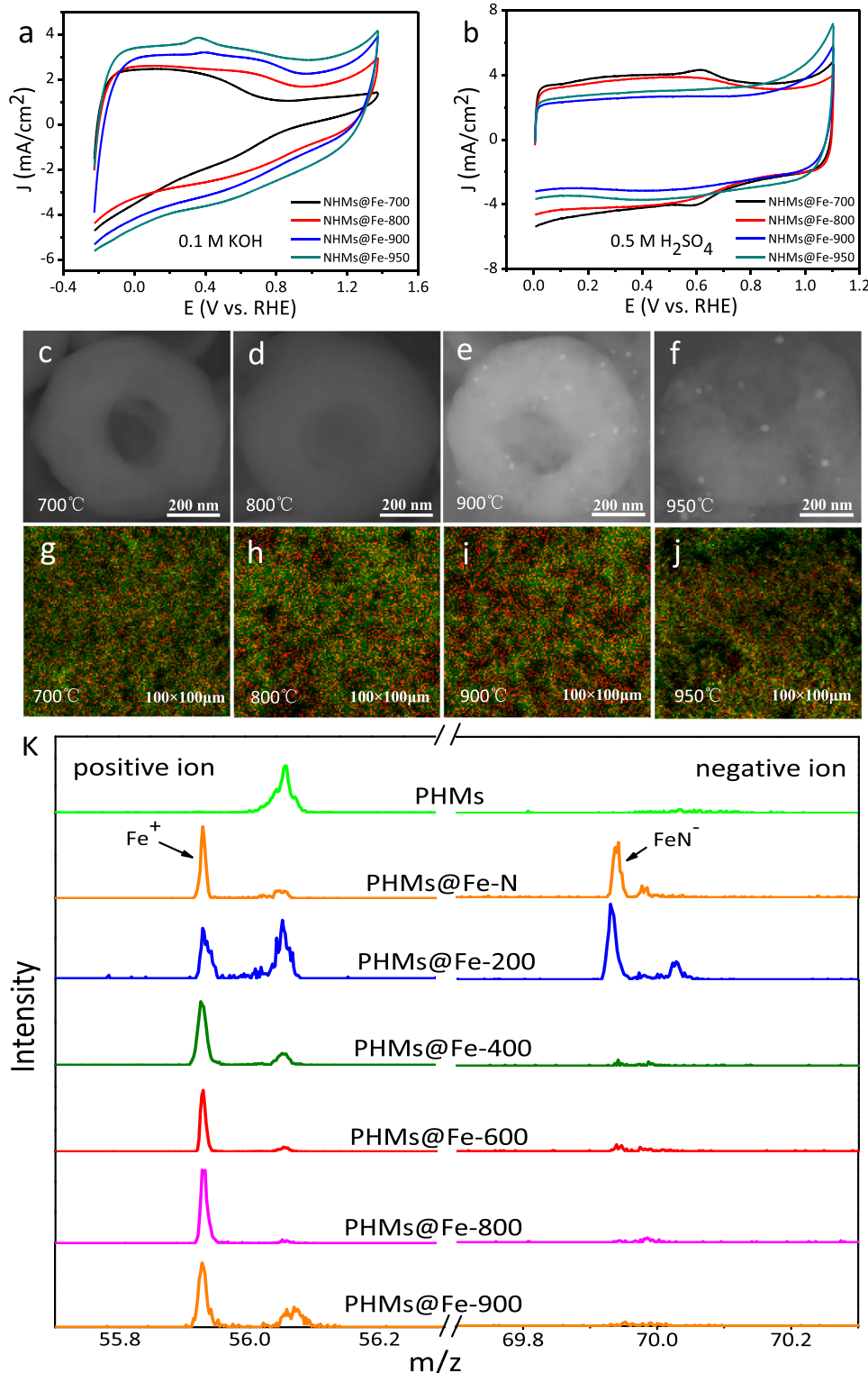


Fig. 4. Surface composition and structure of NHMs@Fe prepared at different temperatures. (a, b) CV curves of NHMs@Fe catalysts prepared at 700, 800, 900 and 950 °C in N_2 -saturated 0.1 M KOH (a) and 0.5 M H_2SO_4 (b). (c-f) SEM images under back-scattering electron detector showing the morphologies and distribution of Fe species (bright spots) in a typical microsphere in NHMs@Fe prepared at 700 °C (c), 800 °C (d), 900 °C (e) and 950 °C (f). (g-j) ToF-SIMS element maps showing the distribution of Fe (red), C (green) on the surface of NHMs@Fe catalysts prepared at 700 °C (g), 800 °C (h), 900 °C (i) and 950 °C (j). (k) High-resolution secondary positive and negative ion spectra of PHMs and PHMs@Fe-N heat-treated at different temperatures.

species were detected [25]. Secondly, we used ToF-SIMS with a surface sensitivity of ~ 10 Å to directly measure the surface composition and molecular structure of NHMs@Fe. Unfortunately, any fragment ions related to Fe-N_x were not detected except fragment ions of iron (Fig. S26b). The structure information obtained by XAS and ToF-SIMS study indicates that there are no Fe-N_x sites in the NHMs@Fe. However, despite the absence of the proposed Fe-N_x active sites, the NHMs@Fe catalyst still exhibits a surprisingly high ORR activity. This suggests the presence of an underlying active site associated with Fe that has not been found.

3.6. Relationship between surface structure and activity with increasing carbonization temperature

To further understand the origin of high activity, we used surface-sensitive techniques to systematically investigate structure-activity relationship of NHMs@Fe catalysts prepared at different temperatures. Because electrochemical reactions always occur on the outermost surface of electrode, an electrochemical method was used to characterize the electrochemical properties of NHMs@Fe catalysts. Cyclic voltammetric (CV) curves of the NHMs@Fe catalysts prepared at 900 °C or above showed a small anodic peak at ~ 0.35 V in alkaline media (Fig. 4a), which correspond to the Fe species observed in Fig. 4e andf. However, a pair redox peaks appeared at ~ 0.6 V in the CV curves of NHMs@Fe catalysts prepared at 800 °C or below in an acidic medium (Fig. 4b), which may be associated with the unobserved Fe species. These results indicate that 900 °C is the key point at which the surface composition mutates. Furthermore, the ORR activities of the NHMs@Fe catalysts in both alkaline and acidic media show a significant increase with an increase in carbonization temperature from 700 °C to 900 °C and have an attenuation at 950 °C (Fig. S24c,d), suggesting that the carbonization temperatures have a significant effect on the catalytic activities.

The catalytic performance of catalysts is mainly determined by their surface structure. Therefore, the surface composition and molecular structure of the NHMs@Fe catalysts prepared at different temperatures were investigated by using ToF-SIMS, as shown in Fig. 4k. The fragment ions of Fe-N can be identified on PHMs@Fe-N obtained at 200 °C or below. However, the fragment ions related to Fe-N_x are not detected on PHMs@Fe-N obtained at 400 °C or above. These results indicate that the Fe-N_x coordination structure originally designed on the surface of the PHMS was not retained as the Fe-N_x active site during synthesis of the catalyst, but in fact the Fe-N bonds are broken at temperatures above 200 °C. Fe ions produced by the cleavage of Fe-N coordination easily combine with oxygen to form iron oxides due to the presence of oxygen during the pyrolysis of the precursor (see Supporting 3, Supporting 4 and Supporting 22). Furthermore, fragment ions of Fe and C-N can always be found in the positive and negative mass spectra from room temperature to 900 °C (Figs. S25b and S27). The presence of C-N fragment ions after the formation of carbon indicates that N atoms enter the sp² carbon lattice to form the N-doped carbon. In addition, XPS results show a significant and sustained decrease of total N content in the N-doped carbon with the increase of carbonization temperature from 700 °C to 950 °C (Table S7).

Based on the principle of element contrast, the morphologies and distribution of iron species of the NHMs@Fe catalysts prepared at different temperatures were further characterized by SEM under a back-scattering electron detector mode, as shown in Fig. 4c-f. None of the images associated with Fe are found on the NHMs@Fe catalysts prepared at 800 °C or below (Fig. 4c, d). However, a few Fe nanoparticles can be observed on the NHMs@Fe catalysts prepared at 900 °C (Fig. 4e), and then more and larger crystalline nanoparticles appear on the NHMs@Fe catalysts prepared at 950 °C (Fig. 4 f), which agrees with the XRD analysis results (Fig. S28). This phenomenon is further confirmed by the ToF-SIMS maps, which indicate that fragment ions related to Fe are homogeneously distributed on the surface of the NHMs@Fe

catalysts. Furthermore, the concentration of fragment ions shows a significant increase with increasing carbonization temperature from 700 °C to 900 °C (Fig. 4g-i), decreasing at 950 °C (Fig. 4j). Most notably, single Fe atoms are not observed by atomic-resolution HAADF-STEM on the NHMs@Fe prepared at 800 °C (Fig. S15c), while single Fe atoms are clearly observed on the NHMs@Fe prepared at 900 °C (Figs. 1i and S15a).

In addition, it is noteworthy that a shift of Fe atoms occurs when the electron beam triggers an Fe atom. The elongated images of single Fe atoms caused by the motion of the Fe atoms are shown in Fig. S16. That the singular Fe atoms diffuse along the graphene edge rather than escape implies that these isolated Fe atoms are incorporated into the carbon rings and have low coordination characteristics, similar to previous observations [45].

Based on the above results, we concluded that (i) the ORR activity increases with increasing carbonization temperature and aren't primarily dependent on total N content, (ii) there are no Fe-N_x coordination structures on the surface of NHMs@Fe catalysts prepared at 700 °C or above, and (iii) low coordination single Fe atoms on the surface of NHMs@Fe catalyst are associated with the highest ORR activity when carbonization temperature is 900 °C, while when the carbonization temperature is 950 °C, there are more Fe atoms agglomeration, resulting in a decrease in ORR activity.

3.7. A new formation mechanism of active sites for ORR

The preparation of NHMs@Fe catalysts first undergoes pyrolysis of PHMs@Fe-N, and then fractions of nitrogen and carbon are integrated into the carbonaceous support, together with atomically dispersed iron, to form the catalytically active centers embedded into the carbon support. In general, this preparation process is considered a carbonization process, but it actually involves a metallurgical process, in which iron oxide is reduced by carbon to iron atoms at high temperatures. According to the equilibrium diagram of iron oxide being reduced in carbon (Supporting 23), single Fe atoms and Fe nanoparticles can appear just as the carbonization temperature reaches or exceeds the initial reduction temperature (~ 900 °C) of iron oxide, thus leading to a sudden change in the surface structure. Furthermore, a remarkable drop of N content in the NHMs@Fe catalysts with carbonization temperature increases indicates that a large number of N atoms are removed from the N-doped carbon. The removal of N atoms from N-doped carbon, as Yao et al. reported [21], creates valuable defects and these defects can also anchor single metal atoms as catalytic sites [46–48].

From these results, we can reasonably infer that when the carbonization temperature of NHMs@Fe is close to the initial reduction temperature of iron oxide (~ 900 °C), the Fe atoms can just be reduced from iron oxides. Because these Fe atoms have very high surface energy, there are only two ways to minimize their surface energy of these Fe atoms: one is that the migration of Fe atoms on the surface of the carbon microsphere causes atomic agglomeration to produce Fe nanoparticles (Fig. 4e), and also catalyzes the conversion of amorphous carbon to graphite carbon [45], the above also leads to the exposure of more plane edges and defects, along with N loss, in good agreement with the results of the Raman and SRPES analyses. The other is that the Fe atoms are directly embedded into carbon defects to form stable single Fe atoms, which has been confirmed by the observation that single Fe atoms only occupy defective sites (Fig. 1h). These defects are lattice vacancies created by the removal of N atoms from the sp² carbon lattice, which is called N-removed vacancy here. Based on the fact that carbon vacancies anchor single metal atoms, a new formation mechanism of active sites is proposed: the single Fe atoms produced through carbothermal reduction are directly trapped into adjacent carbon vacancies generated by the removal of N to create active sites for high ORR performance.

To reveal the catalytic ability of single Fe atoms anchored by carbon defects in ORR, three possible models of N-modified vacancies-anchored single Fe atoms are proposed based on the facts that specific carbon

defect types can be selectively formed by removing N atoms that occupy a particular position in the carbon ring [49], as shown in Fig. 5a. The formation energy of singular Fe atoms anchored by three vacancy types at different sites on the graphene substrate was calculated by density functional theory (DFT), as shown in Fig. 5c. The calculation shows that the Fe atom can be trapped strongly on each substrate due to a negative value of formation energy (all are approximately -0.88 eV), in good agreement with the strong hybridization between the Fe-3d orbit and the 2p orbit of the neighboring C atom (Fig. S32a). Furthermore, there is a 0.74 e $^-$ charge transfer from a single Fe atom to a graphene substrate (Fig. 5b), suggesting that the dispersion of single Fe atoms on the carbon surface is feasible. Because Fe atoms can enter the three types of vacancies to form various sites, the adsorption of oxygenated intermediates (O^* and OH^*) on these sites is investigated. The adsorption free energies of O^* and OH^* for various sites present a scaling relation with a slope of ~ 0.5 (Fig. 5d), which agrees with previous results [50]. Interestingly, site 2 possesses an appropriate adsorption free energy for OH^* of 1.16 eV, implying that site 2 should have outstanding electrochemical activity. Furthermore, we also compute free-energy diagrams of the ORR for pristine graphene and site 2. For pristine graphene, the adsorption of O_2 as OOH^* becomes less energetically favorable, while other subsections remain energetically favorable at $U = 0.57$ V, so the

adsorption of O_2 as OOH^* must be the rate determination step in the ORR, and the minimum ORR overpotential is 0.66 V. For site 2, the formation of OOH^* is associated with the largest change in Gibbs free energy, and its ORR overpotential is only 0.41 V (Fig. 5e), indicating that the graphene vacancy-anchored single Fe atoms possess superior electrocatalytic activity for the ORR.

4. Conclusions

In summary, we confirm that single Fe atoms produced through carbothermal reduction are homogeneously distributed across the N-poor carbon surface to create active sites for ORR. The optimal NHMs@Fe catalyst shows a surprisingly high ORR activity and superior long-term stability in both acidic and alkaline media. Especially, its half-wave potential of 0.912 V (RHE) is the most positive among the current state-of-the-art M-N-C catalyst in alkaline medium. The low coordination single Fe atoms anchored on the carbon vacancies are responsible for high ORR activity. The anchoring effect of N-removed carbon vacancies to single iron atoms indicates that a new formation mechanism of active sites exists in the pyrolyzed Fe-N-C system. Our work clarifies the mechanisms of roles of Fe for the Fe-N-C catalyst in enhancing ORR and presents a new approach to largely maximize Fe catalytic efficiency

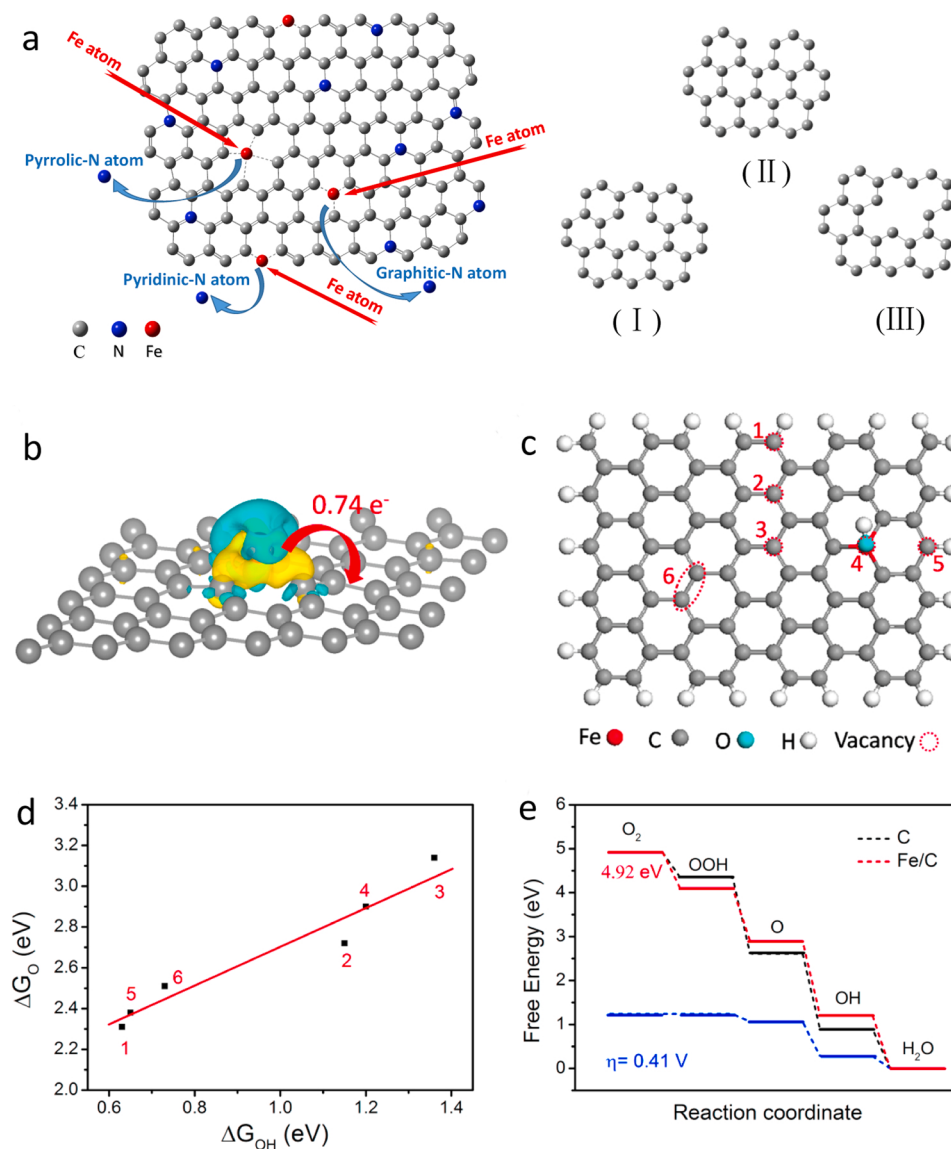


Fig. 5. Theoretical simulations of the catalytic origins. (a) Schematic illustration of a new formation mechanism of active sites. Single Fe atoms produced through carbothermal reduction are respectively embedded into three types of vacancies, including monovacancy (I), edge-vacancy (II) and divacancy (III). These three vacancies are generated by the removal of graphitic-N, pyridinic-N, and pyrrolic-N atoms from carbon basal planes, respectively. (b) Isosurfaces of local charge density difference of carbon defects-anchored single Fe atoms on graphene substrate. (c) The different sites of single Fe atoms anchored by N vacancies on a graphene substrate, in which single Fe atom is linked to an axial oxygen-containing ligand, the N vacancies are mainly including monovacancy (2, 3, 4), edge-vacancy (1, 5), and divacancy (6). (d) Adsorption energies of OH^* versus adsorption energies of O^* on different sites. (e) Comparison of free energy diagram of ORR for pristine graphene and site 2.

with atomic level utilization.

CRediT authorship contribution statement

Feng Tan and Xikun Yang: Conceived and designed the experiments. **Jingsong Wang and Chungang Min:** Carried out the theoretical calculations. **Feng Tan and Wei Li:** Performed the electrochemical experiments and analyzed the electrochemical data. **Bingsen Zhang:** Performed AC-STEM measurements. **Zhanping Li:** Performed ToF-SIMS spectrometry. **Xusheng Zheng:** Performed SRPES measurements and SRPES data analysis. **Liexing Zhou:** Conducted scanning electron microscope measurements. **Qingnan Shi:** Analyzed the experimental data. **Xikun Yang and Feng Tan:** Analysed experimental data and wrote the paper. All authors reviewed and contributed to the manuscript.

Declaration of Competing Interest

The authors declare that they have no known competing financial interests or personal relationships that could have appeared to influence the work reported in this paper.

Acknowledgements

We would like to acknowledge funding support from the National Natural Science Foundation of China (Projects 21363012, 51374117 and 11764026). We thank the BL10B in NSRL for help in characterizations and BL11B in SSRF for XAS measurement.

Appendix A. Supporting information

Supplementary data associated with this article can be found in the online version at [doi:10.1016/j.apcatb.2021.121035](https://doi.org/10.1016/j.apcatb.2021.121035).

References

- [1] S. Zhang, W. Yang, Y. Liang, X. Yang, M. Cao, R. Cao, Template-free synthesis of non-noble metal single-atom electrocatalyst with N-doped holey carbon matrix for highly efficient oxygen reduction reaction in zinc-air batteries, *Appl. Catal. B Environ.* 285 (2021), 119780, <https://doi.org/10.1016/j.apcatb.2020.119780>.
- [2] X. Fu, G. Jiang, G. Wen, R. Gao, S. Li, M. Li, J. Zhu, Y. Zheng, Z. Li, Y. Hu, L. Yang, Z. Bai, A. Yu, Z. Chen, Densely accessible Fe-Nx active sites decorated mesoporous-carbon-spheres for oxygen reduction towards high performance aluminum-air flow batteries, *Appl. Catal. B Environ.* 293 (2021), 120176, <https://doi.org/10.1016/j.apcatb.2021.120176>.
- [3] G. Wu, K.L. More, C.M. Johnston, P. Zelenay, High-performance electrocatalysts for oxygen reduction derived from polyaniline, iron, and cobalt, *Science* 332 (2011) 443–447, <https://doi.org/10.1126/science.1200832>.
- [4] X. Fu, P. Zamani, J.-Y. Choi, F.M. Hassan, G. Jiang, D.C. Higgins, Y. Zhang, M. A. Hoque, Z. Chen, In situ polymer graphenization ingrained with nanoporosity in a nitrogenous electrocatalyst boosting the performance of polymer-electrolyte-membrane fuel cells, *Adv. Mater.* 29 (2017), 1604456, <https://doi.org/10.1002/adma.201604456>.
- [5] Q. Liu, X. Liu, L. Zheng, J. Shui, The solid-phase synthesis of an Fe-N-C electrocatalyst for high-power proton-exchange membrane fuel cells, *Angew. Chem. Int. Ed.* 57 (2018) 1204–1208, <https://doi.org/10.1002/anie.201709597>.
- [6] Y.-C. Wang, Y.-J. Lai, L. Song, Z.-Y. Zhou, J.-G. Liu, Q. Wang, X.-D. Yang, C. Chen, W. Shi, Y.-P. Zheng, M. Rauf, S.-G. Sun, S-doping of an Fe/N/C ORR catalyst for polymer electrolyte membrane fuel cells with high power density, *Angew. Chem. Int. Ed.* 54 (2015) 9907–9910, <https://doi.org/10.1002/anie.201503159>.
- [7] Y. Qiao, P. Yuan, Y. Hu, J. Zhang, S. Mu, J. Zhou, H. Xia, J. He, Q. Xu, Sulfuration of an Fe-N-C catalyst containing FexC/Fe species to enhance the catalysis of oxygen reduction in acidic media and for use in flexible Zn-air batteries, *Adv. Mater.* 30 (2018), 1804504, <https://doi.org/10.1002/adma.201804504>.
- [8] R. Cao, R. Thapa, H. Kim, X. Xu, M.G. Kim, Q. Li, N. Park, M. Liu, J. Cho, Promotion of oxygen reduction by a bio-inspired tethered iron phthalocyanine carbon nanotube-based catalyst, *Nat. Commun.* 4 (2013), 2076, <https://doi.org/10.1038/ncomms3076>.
- [9] Y. Liang, Y. Li, H. Wang, J. Zhou, J. Wang, T. Regier, H. Dai, Co₃O₄ Nanocrystals on graphene as a synergistic catalyst for oxygen reduction reaction, *Nat. Mater.* 10 (2011) 780–786, <https://doi.org/10.1038/NMAT3087>.
- [10] Y. Guo, P. Yuan, J. Zhang, Y. Hu, I.S. Amiinu, X. Wang, J. Zhou, H. Xia, Z. Song, Q. Xu, S. Mu, Carbon nanosheets containing discrete Co-N_x-By-C active sites for efficient oxygen electrocatalysis and rechargeable Zn-air batteries, *ACS Nano* 12 (2018) 1894–1901, <https://doi.org/10.1021/acsnano.7b08721>.
- [11] H. Wu, H. Li, X. Zhao, Q. Liu, J. Wang, J. Xiao, S. Xie, R. Si, F. Yang, S. Miao, X. Guo, G. Wang, X. Bao, Highly doped and exposed Cu(I)-N active sites within graphene towards efficient oxygen reduction for Zn-air batteries, *Energy Environ. Sci.* 9 (2016) 3736–3745, <https://doi.org/10.1039/c6ee01867j>.
- [12] H.T. Chung, D.A. Cullen, D. Higgins, B.T. Sneed, E.F. Holby, K.L. More, P. Zelenay, Direct atomic-level insight into the active sites of a high-performance PGM-free ORR catalyst, *Science* 357 (2017) 479–484, <https://doi.org/10.1126/science.aan2255>.
- [13] W.-J. Jiang, L. Gu, L. Li, Y. Zhang, X. Zhang, L.-J. Zhang, J.-Q. Wang, J.-S. Hu, Z. Wei, L.-J. Wan, Understanding the high activity of Fe-N-C electrocatalysts in oxygen reduction: Fe/Fe₃C nanoparticles boost the activity of Fe-N_x, *J. Am. Chem. Soc.* 138 (2016) 3570–3578, <https://doi.org/10.1021/jacs.6b00757>.
- [14] A. Zitolo, V. Goellner, V. Armel, M.-T. Sougrati, T. Mineva, L. Stievano, E. Fonda, F. Jaouen, Identification of catalytic sites for oxygen reduction in iron- and nitrogen-doped graphene materials, *Nat. Mater.* 14 (2015) 937–942, <https://doi.org/10.1038/nmat4367>.
- [15] W. Cheng, P. Yuan, Z. Lv, Y. Guo, Y. Qiao, X. Xue, X. Liu, W. Bai, K. Wang, Q. Xu, J. Zhang, Boosting defective carbon by anchoring well-defined atomically dispersed metal-N_x sites for ORR, OER, and Zn-air batteries, *Appl. Catal. B Environ.* 260 (2020), 118198, <https://doi.org/10.1016/j.apcatb.2019.118198>.
- [16] X. Xu, Z. Xia, X. Zhang, R. Sun, X. Sun, H. Li, C. Wu, J. Wang, S. Wang, G. Sun, Atomically dispersed Fe-N-C derived from dual metal-organic frameworks as efficient oxygen reduction electrocatalysts in direct methanol fuel cells, *Appl. Catal. B Environ.* 259 (2019), 118042, <https://doi.org/10.1016/j.apcatb.2019.118042>.
- [17] H. Zhang, H.T. Chung, D.A. Cullen, S. Wagner, U.I. Kramm, K.L. More, P. Zelenay, G. Wu, High-performance oxygen reduction reaction fuel cell catalysts exclusively containing atomically dispersed iron active sites, *Energy Environ. Sci.* 12 (2019) 2548–2558, <https://doi.org/10.1039/c9ee00877b>.
- [18] J. Xiao, Y. Xu, Y. Xia, J. Xi, S. Wang, Ultra-small Fe₂N nanocrystals embedded into mesoporous nitrogen-doped graphitic carbon spheres as a highly active, stable, and methanol-tolerant electrocatalyst for the oxygen reduction reaction, *Nano Energy* 24 (2016) 121–129, <https://doi.org/10.1016/j.nanoen.2016.04.026>.
- [19] H. Fei, J. Dong, Y. Feng, C.S. Allen, C. Wan, B. Voloskiy, M. Li, Z. Zhao, Y. Wang, H. Sun, P. An, W. Chen, Z. Guo, C. Lee, D. Chen, I. Shakir, M. Liu, T. Hu, Y. Li, A. I. Kirkland, X. Duan, Y. Huang, General synthesis and definitive structural identification of Mn₄C₄ single-atom catalysts with tunable electrocatalytic activities, *Nat. Catal.* 1 (2018) 63–72, <https://doi.org/10.1038/s41929-017-0008-y>.
- [20] J. Li, L. Jiao, E. Wegener, L.L. Richard, E. Liu, A. Zitolo, M.T. Sougrati, S. Mukerjee, Z. Zhao, Y. Huang, F. Yang, S. Zhong, H. Xu, A.J. Kropf, F. Jaouen, D.J. Myers, Q. Jia, Evolution pathway from iron compounds to Fe_{1(II)}-N_x sites through gas-phase iron during pyrolysis, *J. Am. Chem. Soc.* 142 (2020) 1417–1423, <https://doi.org/10.1021/jacs.9b11197>.
- [21] H. Zhao, C. Sun, Z. Jin, D.-W. Wang, X. Yan, Z. Chen, G. Zhu, X. Yao, Carbon for the oxygen reduction reaction: a defect mechanism, *J. Mater. Chem. A* 3 (2015) 11736–11739, <https://doi.org/10.1039/c5ta02229k>.
- [22] Y. Jia, L. Zhang, A. Du, G. Gao, J. Chen, X. Yan, C.L. Brown, X. Yao, Defect graphene as a trifunctional catalyst for electrochemical reactions, *Adv. Mater.* 28 (2016) 9532–9538, <https://doi.org/10.1002/adma.201602912>.
- [23] X. Wei, X. Luo, H. Wang, W. Gu, W. Cai, Y. Lin, C. Zhu, Highly-defective Fe-N-C catalysts towards pH-universal oxygen reduction reaction, *Appl. Catal. B Environ.* 263 (2020), 118347, <https://doi.org/10.1016/j.apcatb.2019.118347>.
- [24] C. Tang, B. Wang, H.-F. Wang, Q. Zhang, Defect engineering toward atomic Co-N_x-C in hierarchical graphene for rechargeable flexible solid Zn-air batteries, *Adv. Mater.* 29 (2017), 1703185, <https://doi.org/10.1002/adma.201703185>.
- [25] K. Strickland, E. Miner, Q. Jia, U. Tylus, N. Ramaswamy, W. Liang, M.-T. Sougrati, F. Jaouen, S. Mukerjee, Highly active oxygen reduction non-platinum group metal electrocatalyst without direct metal-nitrogen coordination, *Nat. Commun.* 6 (2015), 7343, <https://doi.org/10.1038/ncomms8343>.
- [26] Y. Li, W. Zhou, H. Wang, L. Xie, Y. Liang, F. Wei, J.-C. Idrobo, S.J. Pennycook, H. Dai, An oxygen reduction electrocatalyst based on carbon nanotube-graphene complexes, *Nat. Nanotechnol.* 7 (2012) 394–400, <https://doi.org/10.1038/NNANO.2012.72>.
- [27] J. Masa, W. Xia, M. Muhler, W. Schuhmann, On the role of metals in nitrogen-doped carbon electrocatalysts for oxygen reduction, *Angew. Chem. Int. Ed.* 54 (2015) 10102–10120, <https://doi.org/10.1002/anie.201500569>.
- [28] G. Wang, K. Jiang, M. Xu, C. Min, B. Ma, X. Yang, A high activity nitrogen-doped carbon catalyst for oxygen reduction reaction derived from polyaniline-iron coordination polymer, *J. Power Sources* 266 (2014) 222–225, <https://doi.org/10.1016/j.jpowsour.2014.05.020>.
- [29] Z. Sun, Y. Wang, L. Zhang, H. Wu, Y. Jin, Y. Li, Y. Shi, T. Zhu, H. Mao, J. Liu, C. Xiao, S. Ding, Simultaneously realizing rapid electron transfer and mass transport in jellyfish-like mott-schottky nanoreactors for oxygen reduction reaction, *Adv. Funct. Mater.* 30 (2020), 1910482, <https://doi.org/10.1002/adfm.201910482>.
- [30] M. Kobayashi, H. Niwa, M. Saito, Y. Harada, M. Oshima, H. Ofuchi, K. Terakura, T. Ikeda, Y. Koshigoe, J.-I. Ozaki, S. Miyata, Indirect contribution of transition metal towards oxygen reduction reaction activity in iron phthalocyanine-based carbon catalysts for polymer electrolyte fuel cells, *Electrochim. Acta* 74 (2012) 254–259, <https://doi.org/10.1016/j.electacta.2012.04.075>.
- [31] C.L. Bentley, M. Kang, P.R. Unwin, Nanoscale surface structure-activity in electrochemistry and electrocatalysis, *J. Am. Chem. Soc.* 141 (2019) 2179–2193, <https://doi.org/10.1021/jacs.8b09828>.

- [32] N. Tian, Z.-Y. Zhou, S.-G. Sun, Y. Ding, Z.L. Wang, Synthesis of tetrahedrahedral platinum nanocrystals with high-index facets and high electro-oxidation activity, *Science* 316 (2007) 732–735, <https://doi.org/10.1126/science.1140484>.
- [33] X. Huang, Z. Zhao, L. Cao, Y. Chen, E. Zhu, Z. Lin, M. Li, A. Yan, A. Zettl, Y. M. Wang, X. Duan, T. Mueller, Y. Huang, High-performance transition metal-doped Pt₃Ni octahedra for oxygen reduction reaction, *Science* 348 (2015) 1230–1234, <https://doi.org/10.1126/science.aaa8765>.
- [34] V.R. Stamenkovic, B. Fowler, B.S. Mun, G. Wang, P.N. Ross, C.A. Lucas, N. M. Marković, Improved oxygen reduction activity on Pt₃Ni(111) via increased surface site availability, *Science* 315 (2007) 493–497, <https://doi.org/10.1126/science.1135941>.
- [35] D. Guo, R. Shibuya, C. Akiba, S. Saji, T. Kondo, J. Nakamura, Active sites of nitrogen-doped carbon materials for oxygen reduction reaction clarified using model catalysts, *Science* 351 (2016) 361–365, <https://doi.org/10.1126/science.aad0832>.
- [36] P. Strasser, S. Koh, T. Anniyev, J. Greeley, K. More, C. Yu, Z. Liu, S. Kaya, D. Nordlund, H. Ogasawara, M.F. Toney, A. Nilsson, Lattice-strain control of the activity in dealloyed core-shell fuel cell catalysts, *Nat. Chem.* 2 (2010) 454–460, <https://doi.org/10.1038/NCHEM.623>.
- [37] J. Yuhara, T. Matsui, The Role of nitrogen in the preferential chromium segregation on the ferritic stainless steel (111) surface, *Appl. Surf. Sci.* 256 (2010) 3438–3442, <https://doi.org/10.1016/j.apsusc.2009.12.048>.
- [38] G. Hörz, H. Kanbach, H. Vetter, The influence of surface segregation of oxygen or nitrogen on the decomposition of hydrocarbons on transition metals, *Mater. Sci. Eng.* 42 (1980) 145–153.
- [39] D.M. Koshy, A.T. Landers, D.A. Cullen, A.V. Ievlev, H.M. Meyer III, C. Hahn, Z. Bao, T.F. Jarillo, Direct characterization of atomically dispersed catalysts: nitrogen-coordinated Ni sites in carbon-based materials for CO₂ electroreduction, *Adv. Energy Mater.* 10 (2020), 2001836, <https://doi.org/10.1002/aenm.202001836>.
- [40] T. Palaniselvam, V. Kashyap, S.N. Bhange, J.-B. Baek, S. Kurungot, Nanoporous graphene enriched with Fe/Co-N active sites as a promising oxygen reduction electrocatalyst for anion exchange membrane fuel cells, *Adv. Funct. Mater.* 26 (2016) 2150–2162, <https://doi.org/10.1002/adfm.201504765>.
- [41] W. Li, C. Min, F. Tan, Z. Li, B. Zhang, R. Si, M. Xu, W. Liu, L. Zhou, Q. Wei, Y. Zhang, X. Yang, Bottom-up construction of active sites in a Cu-N₄-C catalyst for highly efficient oxygen reduction reaction, *ACS Nano* 13 (2019) 3177–3187, <https://doi.org/10.1021/acsnano.8b08692>.
- [42] J.-L. Shui, N.K. Karan, M. Balasubramanian, S.-Y. Li, D.-J. Liu, Fe/N/C composite in Li-O₂ battery: studies of catalytic structure and activity toward oxygen evolution reaction, *J. Am. Chem. Soc.* 134 (2012) 16654–16661, <https://doi.org/10.1021/ja3042993>.
- [43] H. Niwa, K. Horiba, Y. Harada, M. Oshima, T. Ikeda, K. Terakura, J. Ozaki, S. Miyata, X-ray absorption analysis of nitrogen contribution to oxygen reduction reaction in carbon alloy cathode catalysts for polymer electrolyte fuel cells, *J. Power Sources* 187 (2009) 93–97, <https://doi.org/10.1016/j.jpowsour.2008.10.064>.
- [44] W. Ding, Z. Wei, S. Chen, X. Qi, T. Yang, J. Hu, D. Wang, L.-J. Wan, S.F. Alvi, L. Li, Space-confinement-induced synthesis of pyridinic- and pyrrolic-nitrogen-doped graphene for the catalysis of oxygen reduction, *Angew. Chem. Int. Ed.* 52 (2013) 11755–11759, <https://doi.org/10.1002/anie.201303924>.
- [45] J. Zhao, Q. Deng, S.M. Avdoshenko, L. Fu, J. Eckert, M.H. Rümmeli, Direct in situ observations of single Fe atom catalytic processes and anomalous diffusion at graphene edges, *PNAS* 111 (2014) 15641–15646, <https://doi.org/10.1073/pnas.1412962111>.
- [46] L. Zhang, Y. Jia, G. Gao, X. Yan, N. Chen, J. Chen, M.T. Soo, B. Wood, D. Yang, A. Du, X. Yao, Graphene defects trap atomic Ni species for hydrogen and oxygen evolution reactions, *Chem* 4 (2018) 285–297, <https://doi.org/10.1016/j.chempr.2017.12.005>.
- [47] J. Liu, M. Jiao, B. Mei, Y. Tong, Y. Li, M. Ruan, P. Song, G. Sun, L. Jiang, Y. Wang, Z. Jiang, L. Gu, Z. Zhou, W. Xu, Carbon-supported divacancy-anchored platinum single-atom electrocatalysts with superhigh Pt utilization for the oxygen reduction reaction, *Angew. Chem. Int. Ed.* 58 (2019) 1163–1167, <https://doi.org/10.1002/anie.201812423>.
- [48] D. Liu, X. Li, S. Chen, H. Yan, C. Wang, C. Wu, Y.A. Haleem, S. Duan, J. Lu, B. Ge, P. M. Ajayan, Y. Luo, J. Jiang, L. Song, Atomically dispersed platinum supported on curved carbon supports for efficient electrocatalytic hydrogen evolution, *Nat. Energy* 4 (2019) 512–518, <https://doi.org/10.1038/s41560-019-0402-6>.
- [49] Y. Jia, L. Zhang, L. Zhuang, H. Liu, X. Yan, X. Wang, J. Liu, J. Wang, Y. Zheng, Z. Xiao, E. Taran, J. Chen, D. Yang, Z. Zhu, S. Wang, L. Dai, X. Yao, Identification of active sites for acidic oxygen reduction on carbon catalysts with and without nitrogen doping, *Nat. Catal.* 2 (2019) 688–695, <https://doi.org/10.1038/s41929-019-0297-4>.
- [50] J.K. Nørskov, J. Rossmeisl, A. Logadottir, L. Lindqvist, J.R. Kitchin, T. Bligaard, H. Jónsson, Origin of the overpotential for oxygen reduction at a fuel-cell cathode, *J. Phys. Chem. B* 108 (2004) 17886–17892, <https://doi.org/10.1021/jp047349j>.